

Convolutional neural networks applied to the interpretation of lineaments in aeromagnetic data

Tomas Naprstek¹ and Richard S. Smith²

ABSTRACT

Parameter estimation in aeromagnetics is an important tool for geologic interpretation. Due to aeromagnetic data being highly prevalent around the world, it can often be used to assist in understanding the geology of an area as a whole or for locating potential areas of further investigation for mineral exploration. Methods that automatically provide information such as the location and depth to the source of anomalies are useful to the interpretation, particularly in areas where a large number of anomalies exist. Unfortunately, many current methods rely on high-order derivatives and are therefore susceptible to noise in the data. Convolutional neural networks (CNNs) are a subset of machine-learning methods that are well-suited to image processing tasks, and they have been shown to be effective at interpreting other geophysical data, such as seismic sections. Following

several similar successful approaches, we have developed a CNN methodology for estimating the location and depth of lineament-type anomalies in aeromagnetic maps. To train the CNN model, we used a synthetic aeromagnetic data modeler to vary the relevant physical parameters, and we developed a representative data set of approximately 1.4 million images. These were then used for training classification CNNs, with each class representing a small range of depth values. We first applied the model to a series of difficult synthetic data sets with varying amounts of noise, comparing the results against the tilt-depth method. We then applied the CNN model to a data set from northeastern Ontario, Canada, that contained a dike with known depth that was correctly estimated. This method is shown to be robust to noise, and it can easily be applied to new data sets using the trained model, which has been made publicly available.

INTRODUCTION

Assisted interpretation of aeromagnetic data is a well-researched field, with many methods being developed since aeromagnetics was introduced as a geophysical tool. The reasoning initially was to aid geophysicists and geologists in interpreting data; however, in more recent years this has expanded to include the fact that there are now more aeromagnetic data collected than are reasonable to be interpreted manually. As such, automated and semiautomated methods are increasingly useful, either to focus interpreters onto specific locations for detailed analysis, or for advanced interpretation that may not be feasible when observing aeromagnetic data over a large area. There are several studies (e.g., Phillips, 2000; Fairhead and Williams, 2006; Pilkington and Keating, 2009; Pilkington and Tschirhart, 2017) that summarize and compare many of the most popular analysis techniques used in aeromagnetics, covering methods such as the vertical derivative (Hood, 1965), analytic signal (Nabighian,

1972; Roest et al., 1992), Euler deconvolution (Thompson, 1982; Reid et al., 1990; Reid and Thurston, 2014), tilt angle (Miller and Singh, 1994; Verduzco et al., 2004; Salem et al., 2007, 2008), and local wavenumber (Thurston and Smith, 1997; Salem et al., 2005). These methods are used for a variety of purposes, ranging from the visual enhancement of structural features, to determining source parameters such as the depth to the top of a source body. Many of these methods are still being built upon, and entirely new approaches are also being developed for edge detection/structure mapping (e.g., some examples from the past 10 years include Cascone et al., 2012; Holden et al., 2012; Lee et al., 2012; Ferreira et al., 2013; Hidalgo-Gato and Barbosa, 2015; Tschirhart and Morris, 2015; Foks and Li, 2016; Sun et al., 2016; Oliveira et al., 2017; Nathan et al., 2020) and source parameter estimation (e.g., some examples from the past 10 years include Ulla et al., 2010; Cooper, 2012, 2014, 2015; Curto et al., 2015; Tontini et al., 2018; De Souza

Manuscript received by the Editor 20 October 2020; revised manuscript received 22 June 2021; published ahead of production 22 September 2021; published online 11 November 2021.

¹National Research Council Canada, Ottawa, Ontario K1A 0R6, Canada. E-mail: tomas.naprstek@nrc-cnrc.gc.ca (corresponding author).

²Laurentian University, Sudbury, Ontario P3E 2C6, Canada. E-mail: rssmith@laurentian.ca.

et al., 2020). Many of these involve high-order derivatives, which may be susceptible to noise in the data.

Due to the continually lowering barrier for entry of usage, machine-learning methods are being applied increasingly in a wide array of applications. Online resources and coding libraries in high-level languages such as Python and R are enabling nonexperts (in machine learning) to train machine-learning models in their own specialized fields. One of the most popular machine-learning methods has been neural networks (NNs), which have been shown to be highly effective at a large number of various data-processing and analysis tasks, including many within the geophysics field (e.g., see summaries such as Poulton, 2002; Peters et al., 2019; Saikia et al., 2020). When implemented as supervised methods, they take data with a predetermined solution (known as labeled data) into their input layer, and they iteratively adjust weightings in “hidden” layers between it and the output layer. This iterative adjustment, known as training, allows the weights to be “learned,” such that when the labeled data are input, the output is close to the expected result. Once trained, the model containing the set of learned weights may be applied to unlabeled data, resulting in predictions for these new data. Convolutional NNs (CNNs) are a further subset of machine-learning methods, whose primary use is for image and video data input (Figure 1). The CNN layers contain images (or matrices), and the weights are convolutional filters of a user-defined size. In the context of geophysics, CNNs have been effective with seismic data, used for applications such as fault detection (e.g., some recent papers include Pochet et al., 2018; Zhang, et al., 2019; Cunha et al., 2020), salt classification (e.g., Waldeland and Solberg, 2017; Shi et al., 2018), and horizon tracking (Yang and Sun, 2020). They have also been used with success in electromagnetics (e.g., Puzyrev and Swidinsky, 2021). In aeromagnetics, Nurindrawati and Sun (2020) use CNNs to estimate the total magnetization direction of anomalies, and Aghaee Rad (2019) applies CNNs to aeromagnetic, gravity, and elevation data to determine geologic lineament locations.

The CNN model architecture comprises several specific components, such as convolutional layers, pooling layers, dropout layers, dense layers, activation functions, and the optimization algorithm. Each of these must be experimented with because no single architecture is appropriate across all applications. Convolutional layers are the primary method in which the CNN functions, developing the weights that will iteratively improve the final output. Of key importance to

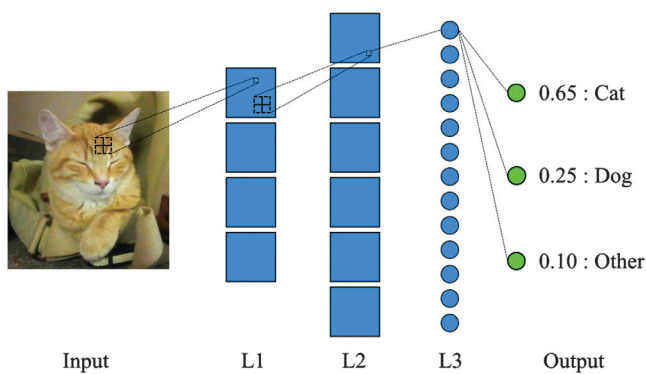


Figure 1. A simple model showing a generic CNN, in which an image is given as the input, three hidden layers process the input, and the output is a probability for each of three possible classes. L1 and L2 could be convolutional or pooling layers, whereas L3 represents a

them is the user-defined kernel size, which determines how large of a convolutional filter to apply to the input matrix. Pooling layers (e.g., Riesenhuber and Poggio, 1999; Scherer et al., 2010; Krizhevsky et al., 2012) apply a small moving window to the output from a previous convolutional layer in an effort to reduce the spatial size (and therefore processing time) while still retaining pertinent information. Max pooling, which keeps the maximum value in each window, and average pooling, which returns the mean of the window, are the two most common pooling filters. Dropout layers (Srivastava et al., 2014) are a standard approach to reduce overfitting the CNN model to the training data, which is a common problem in deep learning. By removing, or “dropping,” a set number of random nodes in a layer, the CNN model is forced to become more robust and not rely on a select few features to analyze an entire data set/image. Activation functions are essentially logistic gates that aim to assist in normalizing neurons and introduce nonlinearity to the CNN (Bishop, 1995). They are applied after every layer in the CNN, including at the final output; however, each layer’s activation function does not need to be the same and can vary depending on the circumstances of the model and application. Dense/fully connected layers in the context of CNNs refer to the standard approach of converting the multidimensional image to a vector (flattening) before the final stages of the CNN model. In most CNN models, several convolutional layers will be part of the CNN model’s analysis, before one or more dense layers are added to output the final result of the model. The optimization algorithm (Bishop, 1995) controls the overall “learning” that the NN accomplishes. It determines how the error is minimized during training, based on a user-defined loss function, calculated between the CNN model’s predicted values and the training data’s true values.

In this research, we applied CNNs to the problem of aeromagnetic data interpretation in the context of dikes, which appear as thin, linear features. Dikes, and dike swarms, generally appear very strongly in aeromagnetic maps, and they can greatly assist in the geologic interpretation of a region (Ernst et al., 1995; Pilkington and Roest, 1998). As such, automatic interpretation methods that can be applied to dikes, such as those mentioned above, are of practical use to many different applications. Of primary interest to us was determining the location and depth to the top of the source of the lineaments. Our approach was to use a synthetic aeromagnetic modeler to generate an extensive data set that changed relevant physical parameters and use it to train a CNN model to predict these parameters in new data, whether synthetic or real. We begin by describing our method for generating the synthetic data used for training and the physical parameters varied to ensure a robust data set. This is followed by a description of the architecture used in our CNN model. We then apply the trained model to a difficult synthetic data set with varying levels of noise to determine the capabilities of the method as well as its resiliency to noise in the data. Finally, we test the effectiveness of the method on a real-world aeromagnetic data set that includes a previously researched dike in northern Ontario, Canada, whose location and depth are known. For comparison in all data sets, we also apply tilt depth as an established and successful aeromagnetic depth estimator.

METHODS

Synthetic training data generation

Because CNNs require a significant amount of labeled training data, the first step of this research was to develop a streamlined approach of generating useful synthetic aeromagnetic data. To

accomplish this, we used GRAV_MAG_PRISM, a MATLAB ([The Mathworks Inc., 2020](#)) program developed by [de Barros et al. \(2013\)](#). The primary reasoning for using this code was that it could be incorporated into a MATLAB script, allowing for the automatic generation of a significant number of combinations of the relevant physical parameters: strike, depth, width, and susceptibility. Although not evaluated as parameters in this study, width and susceptibility were varied to ensure a diverse range of resulting realistic data sets for training. A suite of models was developed, and all of the relevant parameters were assigned a range of values (Table 1). Note that the strike is measured clockwise from the positive easting direction, such that 90° is along the negative northing direction. In addition, all dikes extend infinitely in their length.

This approach also makes three key assumptions to limit the number of variables for training. First, all data were generated with an inclination of 90° and declination of 0°. This means that the trained CNN model will only be appropriate for data that have been reduced to pole. However, because this is a common process, this should not be an issue for most aeromagnetic data sets, unless they are at low latitudes ([Blakely, 1996](#)). In those cases, it should be possible to invert this approach, such that it is trained to use reduced-to-equator data. The second assumption was that no dip variation in the dikes was introduced; therefore, all are assumed to be vertically dipping. Allowing changes in the dip angle would introduce another major variable that would need to be controlled and ideally estimated. Many dikes in Canada do not significantly deviate from a vertical dip ([Bates and Halls, 1990](#); [Ruffman and Greenough, 1990](#); [Tschart and Morris, 2012](#); [Ernst, 2014](#)), so we believed this to be a valid assumption for this approach (R. E. Ernst, personal communication, 2019). The final assumption was that the CNN models could be trained on noise-free data. The expectation was that, even with no noise introduced into the training data, the final trained models would be able to handle expected noise values found within real data sets.

All of the data sets were sampled at a grid spacing of 25 m, with *x* and *y* extents of 500 m, resulting in 21 × 21 cell “windows.” This window size was chosen because it was expected that it would be large enough to contain enough of any lineament to be interpretable when placed in the center of the window. Two additional factors were added in to ensure a robust and varied training data set: a secondary “off-center” lineament with the same properties as the primary lineament and a background rectangular anomaly with a susceptibility of 1/100th that of the primary lineament. As such, every combination of physical parameter values had four resulting data sets: the single primary lineament (Figure 2a), two lineaments (Figure 2b), the primary lineament with a background anomaly (Figure 2c), and the combination of the two lineaments with the background anomaly (Figure 2d). After generating the data set, the location of the lineament was pulled from the GRAV_MAG_PRISM script, and a check was completed to determine if the lineament’s physical size fell within any of the nine center cells of the image (Figure 3a). If it did, then the data set was determined to be a “hit” (e.g., all images in Figure 2 are “hits”), whereas any that do not meet these criteria were labeled as “no lineament” (Figure 3b). This synthetic data generation led to 365,904 individual synthetic aeromagnetic

data sets/images to be used for training. Following standard approaches for training data augmentation (e.g., [Simard et al., 2003](#); [Krizhevsky et al., 2012](#)), these images were then rotated by 90°, 180°, and 270° to garner an additional 1,097,712 images. Finally, 1350 images of generic block-like anomalies without any lineaments present were also generated and added to the no lineament data set. Therefore, the final total data set for training comprised 300,608 images that were labeled as a hit and 1,164,358 images that were labeled as no lineament, totaling 1,464,966 training images. Following standard machine-learning practice, this amount was randomly split, resulting in 67% of the data used for training and the remaining 33% used for validation. The final step before being input into the CNN models for training was to normalize each cell of the images:

$$d_n(x, y) = \frac{d(x, y) - \mu}{\sigma}, \quad (1)$$

where $d(x, y)$ is a single cell’s value, μ is the mean of the image, and σ is the standard deviation of the image. This was done to ensure that simple shifts in the background total field would not affect the final result; instead, all training would focus on the change in shape and size due to the physical parameters varying.

CNN architecture

The depth estimator was trained as a CNN model, implemented in Python using TensorFlow ([Abadi et al., 2015](#)). The model was treated as a multiclassification problem, in which “bins” of depth values were set as separate classes (Table 2), similar to the successful approach by [Nurindrawati and Sun \(2020\)](#). Although regression models would in theory be more appropriate for predicting depth, a continuous variable, this classification model approach requires fewer training data than equivalently robust regression models.

The process of determining the architecture of any NN is highly exploratory, and it depends greatly on the specific data and context it is being applied to. We tested several different architectures (Table 3), as well as varied the optimization algorithm (stochastic gradient descent and Adam) and the number of epochs. We concluded that an architecture very similar to the one described in [Cunha et al. \(2020\)](#) was most effective for our problem, indicated by * in Table 3. In this architecture, we used stochastic gradient descent as our optimization algorithm, with the learning rate set to 0.001 and our loss as “sparse categorical cross entropy” ([TensorFlow, 2020](#)). The rectified linear unit (e.g., [Nair and Hinton, 2010](#)) was used as our activation

Table 1. A list of the physical parameters varied within GRAV_MAG_PRISM.

Parameter (units)	Values
Susceptibility (SI units)	0.001, 0.005, 0.01, 0.05, 0.1, 0.5, 1
Width (m)	5, 9.5, 14, 18.5, 23, 27.5, 32, 36.5, 41, 45.5, 50
<i>x</i> position (m)	50, 150, 250
<i>y</i> position (m)	50, 150, 250
Depth to top (m)	30, 60, 90, 120, 150, 180, 210, 240, 270, 300, 330
Strike (°)	0, 15, 30, 45, 60, 75, 90, 105, 120, 135, 150, 165

function for all convolutional and dense layers because it has been shown to accelerate the training process (e.g., Krizhevsky et al., 2012). The exception to this was the final output layer where a softmax activation (e.g., Bishop, 1995) was used, which produces a normalized probability that suits our treatment of this problem as a multiclassification model. Thus, the final output after the softmax function was a probability for each possible class, the sum of all probabilities being equal to one. The TensorFlow implementation of CNNs also contains an option for class weighting in imbalanced data sets. Through experimentation, it was found to be marginally beneficial to set the “no lineament present” class to 10% (while leaving all other classes at 100%), thus introducing a bias of the training process toward hit data. The model was trained for 75 epochs, with each epoch taking approximately 270 s to complete using TensorFlow’s GPU implementation on a standard desktop using an NVIDIA

GTX 1050Ti graphics card with 4 GBs of RAM. The resulting accuracy and loss plots are shown in Figure 4. At the end of training, the model achieved more than 95% accuracy on the training data and the validation data. The trained model can be downloaded on Tomas Naprstek’s public GitHub.

Application to real data sets and comparison method

Because all of the training data were 21×21 cell images, any image that was to be classified by the model had to be analyzed using this window size. To achieve this on a full data set, a sliding window approach was developed. A window of 21×21 cells would be pulled from the data set, and the central pixel of the window would be analyzed and predicted its respective classification (Figure 5), similar to the approach in Cunha et al. (2020). The

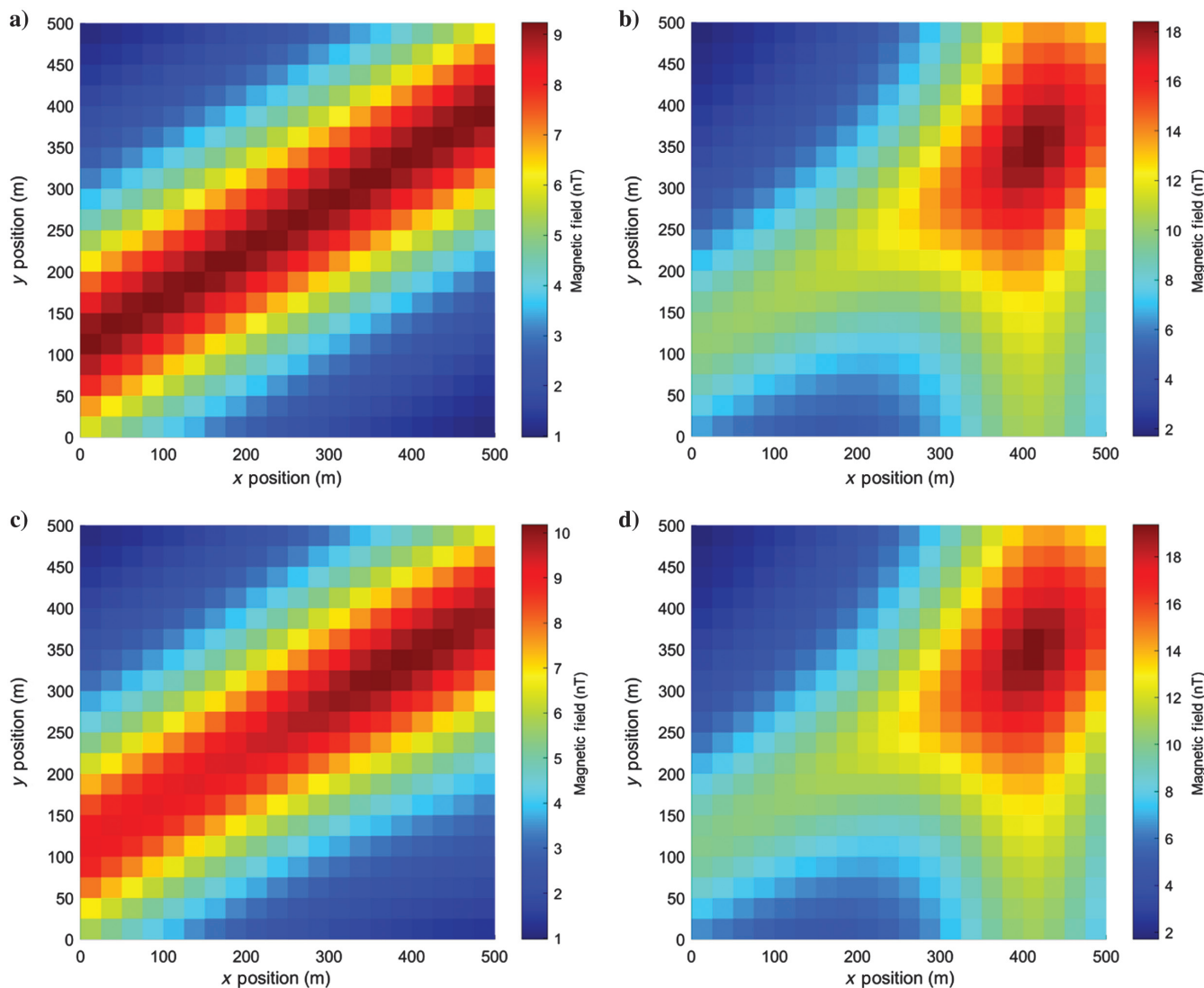


Figure 2. Examples of the synthetic data for training. (a) A lineament passing through the center of the image. It was generated with a susceptibility of 0.01, a width of 14 m, x and y positions of 250 m, a depth to top of 120 m, and a strike of 120°. (b) The same lineament as in (a), but with a secondary identical lineament passing in the $\pm y$ -direction horizontally offset from the primary lineament. (c) The same lineament as in (a) with an additional background anomaly in the upper-right corner. (d) A combination of (b and c) with the additional lineament and the background anomaly.

window would then slide to the next cell, repeating the process until all cells of the data set were analyzed. The image for each sliding window was normalized using the same method as the training data.

To properly evaluate the CNN method's results, one of aeromagnetic's standard depth estimation methods, tilt depth, was also used. The tilt angle is calculated by

$$\theta = \tan^{-1} \left[\frac{\partial M}{\partial z} / \sqrt{\left(\frac{\partial M}{\partial x} \right)^2 + \left(\frac{\partial M}{\partial y} \right)^2} \right], \quad (2)$$

where M is the magnetic field, and the depth estimates are found by measuring the distance between the angle contours (e.g., Salem et al., 2007; Cooper, 2012).

RESULTS

Synthetic data

The CNN model was first applied to a difficult synthetic data set generated using GRAV_MAG_PRISM (Figure 6) with varying levels of Gaussian noise (Figure 7). The data set had a cell size of 25×25 m and a total extent of 5000×5000 m. It contained six lineaments and two background block anomalies whose physical specifications can be found in Table 4. The values in the table were chosen because they contain multiple instances that are at, or near, the split point between bins, therefore making this a particularly difficult data set for the CNN model to estimate. The data set was developed with an inclination of 90° , a declination of 0° , and a background field of 50,000 nT.

The CNN model took approximately 7 s to process each data set, and the results are shown in Figure 8. The results for each lineament were measured, and the distribution of predictions across the 10 depth bins was calculated. For the tilt-depth results

(Figure 9), the physical distance between contours of the tilt angle was measured at several locations along each lineament, leading to a range of depth solutions. The results for both depth estimators applied to each of the four synthetic data sets are recorded in Table 5. At the lowest noise level, both methods were mostly accurate in their depth predictions. The tilt depth method underestimated the depths to L2, L3, and L4 by up to 30 m. However, this is still very accurate, particularly in the context of the CNN method's 25 m bin range. The CNN method underestimated L6 by one bin, due to the depth value (130 m) being close to a bin transition. In addition, the CNN method had some difficulty identifying L4, partially as it has the weakest relative magnetic response of the source models, but primarily because it had the greatest interference with the other lineaments (it interacts with all other lineaments in the

Table 2. The value ranges for each bin in the classification CNN model.

Bin	Depth range (m)
1	0–25
2	26–50
3	51–75
4	76–100
5	101–125
6	126–150
7	151–175
8	176–200
9	201–225
10	226+
11	No lineament present

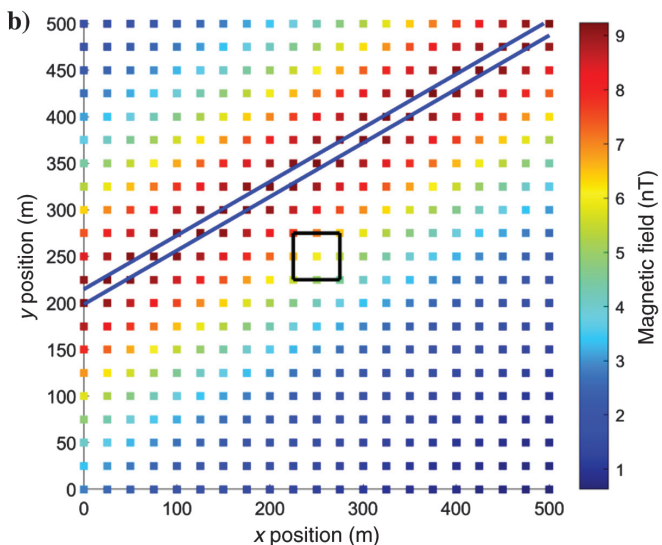
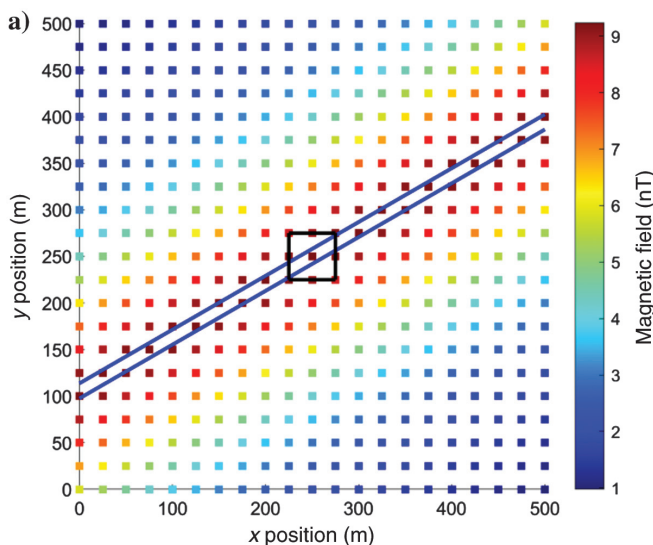


Figure 3. (a) The same data set as in Figure 2a, with each cell separated to show the positioning of the data. The blue lines are the location of the lineament in GRAV_MAG_PRISM, and the black box shows where the check is made to determine if the data set is a hit. (b) The same lineament as in (a), but shifted to a y position of 350 m such that it no longer passes through any of the center nine cells of the image (no lineament).

model). However, L1, L2, and L3 have high confidence values (>75%) for their correctly predicted lineaments. At the 1 nT noise level, the results are mostly identical to the 0.1 nT data set, with the primary difference being that L4 is more difficult to properly measure using the tilt-depth method. CNN method results vary little between 0.1 and 1 nT noise levels. Results begin to change at the 3 nT noise level, with percentage distributions of the CNN method beginning to vary, and lineaments being more difficult to measure with the tilt-depth method due to noise. L4 and L5 become unmeasurable by the tilt-depth method at this point, L4 is less obvious as a feature within the CNN results, and L5 is incorrectly shifted up one bin in the CNN method. Finally, the 10 nT noise data set is entirely unusable with the tilt-depth method due to the extreme noise values. Likewise, the CNN method is unable to detect L4 and L5, whereas all other lineaments suffer in their depth estimations. However, depth estimates for L1, L3, and L6 (still one bin off from the correct value) remain consistent despite the high noise values. Comparing the two solutions against each other, it is clear that the tilt depth is extremely effective at the 0.1 nT noise level, and it is still very accurate at the 1 nT noise level. The CNN method is also accurate at these levels, but it suffers some uncertainty due to the 25 m bin range. However, the CNN method is more robust to the increasing noise level, including the large 3 and 10 nT levels where it continues to accurately predict the depths for the strongest features. As such, it can be concluded that the CNN method should be accurate and resilient to noise in most circumstances. As per the Geological Survey of Canada standards for aeromagnetic surveys (Coyle et al., 2014), the noise must be well below the larger values used here (Reeves, 2005). For instance, Smith and Salem (2005) suggest that Gaussian noise of 0.1 nT would be a typical value in an aeromagnetic survey, with higher values being uncommon, but this is valuable for testing the stability of depth estimator methods.

Table 3. A list of different architectures explored during training.

Number of layers	Architecture details
5	Conv2D(64), Conv2D(64), Flatten, Dense(64), Dense(11)
5	Conv2D(11), Max Pool, Flatten, Dense(22), Dense(11)
6	Conv2D(64), Max Pool, Conv2D(64), Flatten, Dense(64), Dense(11)
6	Conv2D(32), Max Pool, Conv2D(64), Flatten, Dense(64), Dense(11)
6	Conv2D(64), Max Pool, Conv2D(128), Flatten, Dense(128), Dense(11)
6	Conv2D(128), Max Pool, Conv2D(256), Flatten, Dense(256), Dense(11)
8	Conv2D(64), Max Pool, Conv2D(128), Max Pool, Conv2D(128), Flatten, Dense(128), Dense(11)
8	Conv2D(16), Drop(20%), Max Pool, Conv2D(32), Flatten, Dense(32), Drop(20%), Dense(11)
8	Conv2D(32), Drop(20%), Max Pool, Conv2D(64), Flatten, Dense(64), Drop(20%), Dense(11)
8	Conv2D(64), Drop(20%), Max Pool, Conv2D(128), Flatten, Dense(128), Drop(20%), Dense(11)
10	Conv2D(64), Drop(20%), Max Pool, Conv2D(128), Drop(20%), Conv2D(128), Flatten, Dense(128), Drop(20%), Dense(11)
15*	Conv2D(20), Drop(5%), Conv2D(20), Drop(5%), Max Pool, Conv2D(50), Drop(10%), Conv2D(50), Drop(10%), Max Pool, Flatten, Dense(16), Drop(20%), Dense(32), Dense(11)
15	Conv2D(50), Drop(5%), Conv2D(50), Drop(5%), Max Pool, Conv2D(100), Drop(10%), Conv2D(100), Drop(10%), Max Pool, Flatten, Dense(32), Drop(20%), Dense(64), Dense(11)

All Conv2D layers used 3×3 kernels, and all Max Pooling layers used 2×2 kernels. In all Conv2D layers, the padding was set to “same” and the stride was 1. The numbers of filters (for Conv2D) and neurons (for Dense) in each layer are shown in parentheses. Note that the second-to-last architecture (indicated by a *) was the one used in this study.

CASE STUDY

To confirm the effectiveness of this method on real data, it was applied to the Matheson data set from northern Ontario, Canada (Ontario Geological Survey, 2003). This survey was flown N30°W, approximately perpendicular to the local geologic strike, at a line spacing of 200 m, with the magnetic sensor in a bird approximately 70 m above ground. As per the Geological Survey of Canada’s requirements, the survey’s noise envelope that did not

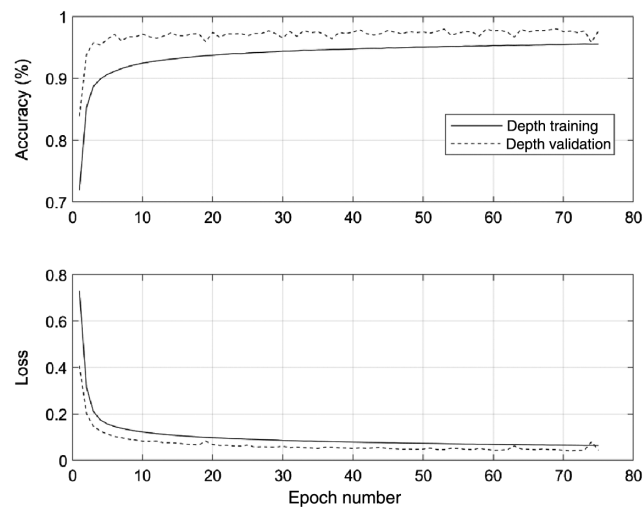


Figure 4. Accuracy and loss plots from the training process for the model. Following a standard practice of a 67%–33% training/validation split of the total data set (1,464,966 images), 981,527 images were used for training and 483,439 images were used for validation.

exceed 0.1 nT. This data set that was chosen as a specific location in the survey area has been analyzed by several other studies (Vallée et al., 2004; Salem et al., 2005; Thurston and Smith, 2007) for dike depth, and, as such, those results can be used for comparison. In addition, the data set includes borehole data that were collected close to the analyzed location, indicating a depth of 41 m to the top of the magnetic body. Therefore, it is expected that the depth should be approximately 111 m below the sensor. However, all three studies, using profile data, estimated a larger depth, ranging from 139 to 145 m. A portion of the total Matheson data set was extracted, centered on the analyzed dike location (Figure 10). It was interpolated at a 40 m cell size using multitrend gridding (Naprstek and Smith, 2019) and reduced to pole using Oasis Montaj (Geosoft, 2020). The 40 m gridded data were then subsampled to 25 m before being input to the CNN models to keep the input data the same size as the data the models were trained on. The specific location of interest (E519470 m, N5377100 m) is circled in the center of the map.

For additional comparisons between the CNN model and the tilt-depth method, seven other dike locations were also analyzed. These additional locations, while not being confirmed by any ground measurements, were added to better understand the CNN model's accuracy when compared to an industry-standard depth estimation technique.

The CNN model took approximately 28 s to predict the data set, and Figure 11 shows the results with the eight locations of interest circled. The contoured tilt angle result is shown in Figure 12, with the eight locations of interest circled. Table 6 lists the results for both methods at these eight locations. Both methods correctly identify and estimate the depth of the dike in the center of the image (E519470 m, N5377100 m), with the CNN model predicting a depth in the 100–125 m bin and the tilt-depth method resulting in a very accurate 106 m depth estimate. The seven other dike depth estimates show that the CNN method is able to predict and agree with the established method of tilt depth. This is highlighted by the

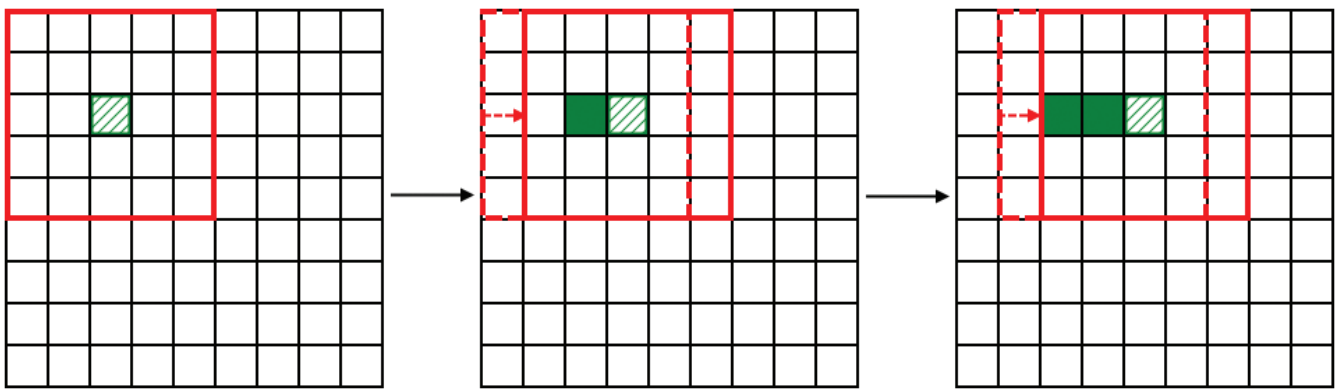


Figure 5. An example (not to scale) of the sliding window approach used in this method. The grid represents the full data set being analyzed, the solid red box is the current window of data being used by the CNN method, and the dashed green cell is the center of the current window. Once analyzed, a class will be assigned to the central cell (solid green), and the window then slides over a cell to repeat the process.

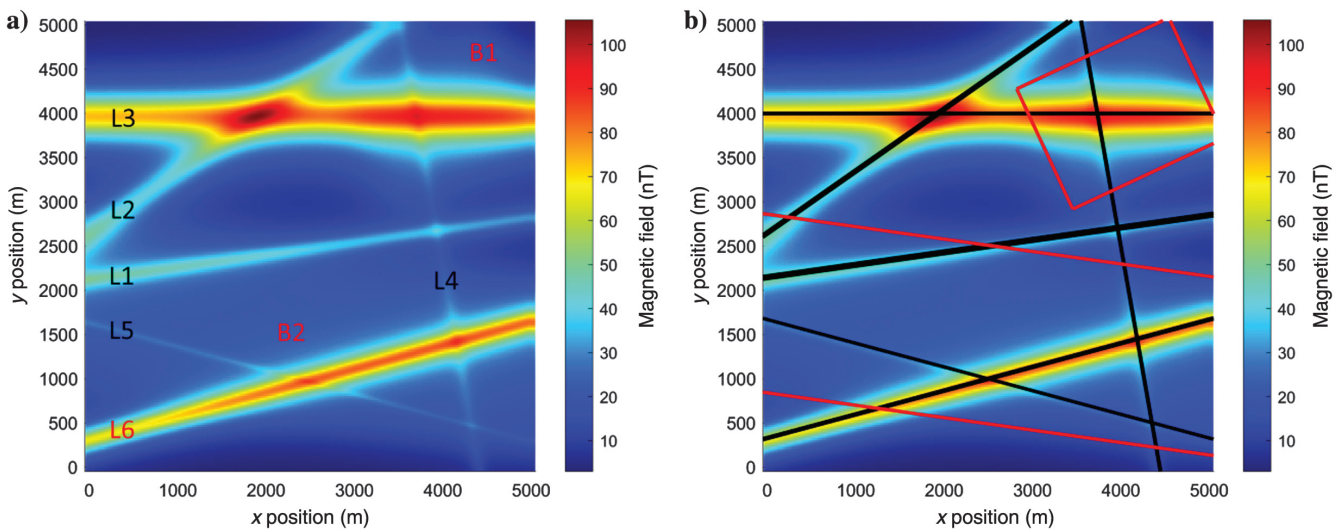


Figure 6. (a) The synthetic model used for testing. The six lineaments being analyzed have been labeled "L1" to "L6" and the two background block anomalies have been labeled "B1" and "B2." (b) The model with the lineaments (in black) and blocks (in red) shown to indicate their physical locations.

multiple measurements along the same lineament, such as the two locations in the northwest, which show that the CNN method can detect the small changes in depth found by the tilt-depth method.

DISCUSSION

We believe that the CNN approach, while computationally intensive and time-consuming to train the initial model, offers a great deal to the potential-field community. Once an effective model has been trained, it can be readily applied to a new data set with no onus on the interpreter to specify additional parameters (as in Euler deconvolution) or perform significant additional manual steps. Therefore, we see the CNN model as an efficient and accurate first-pass approach for noisy or particularly large data sets, immediately presenting the user with potential areas for expert-based interpretation. A trained model is small (the trained depth model used here is <500 KBs), so it can be readily given to other interpreters to use for their own data or to use for their own training and subsequent application with transfer learning. However, in general, the customizability of the established and successful methods

is a positive aspect in the minds of many interpreters because it allows them to inject their expertise and knowledge into the interpretation of the geophysical data. This is something that is less simply done in

Table 4. Specifications of the physical parameters for each anomaly in the synthetic model.

Anomaly	Susceptibility (SI units)	Width (m)	Depth to top (m)
L1	0.01	33	100
L2	0.03	25	185
L3	0.46	5	248
L4	0.008	8	80
L5	0.014	2	35
L6	0.07	15	130
B1	0.001	N/A	300
B2	0.001	N/A	300

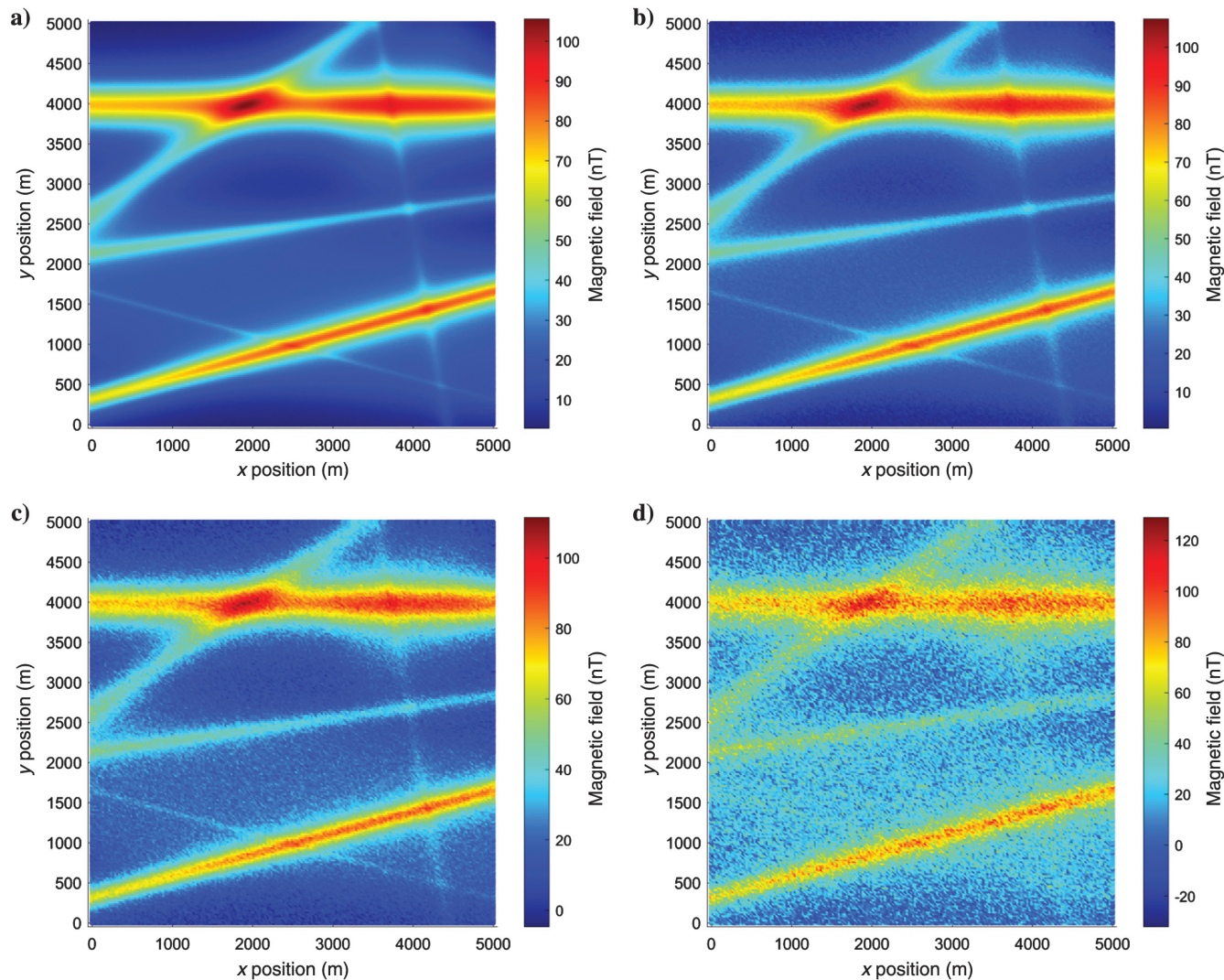


Figure 7. The synthetic data set with varying noise levels: (a) 0.1 nT, (b) 1 nT, (c) 3 nT, and (d) 10 nT.

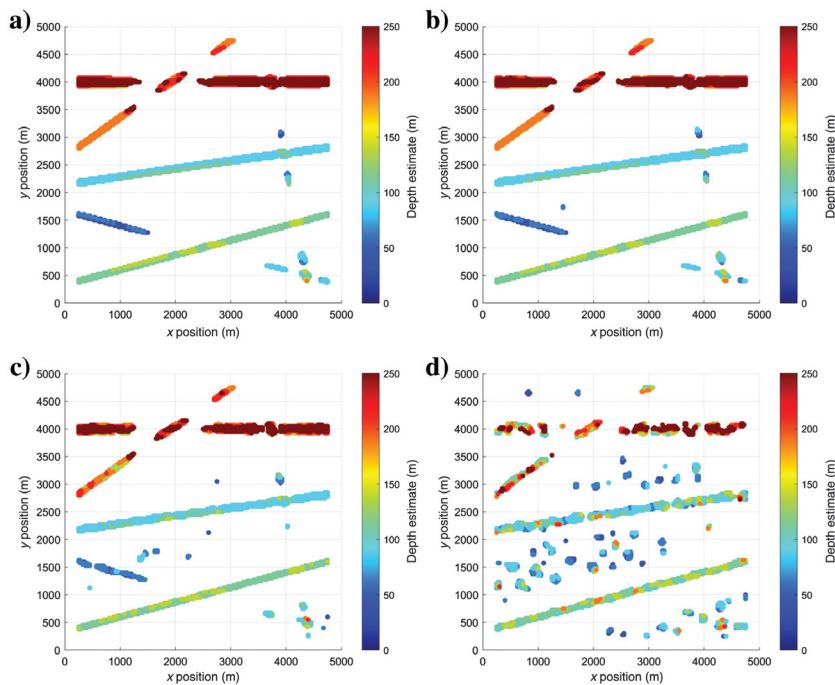


Figure 8. The CNN model results of the synthetic data sets with increasing noise levels: (a) 0.1 nT, (b) 1 nT, (c) 3 nT, and (d) 10 nT.

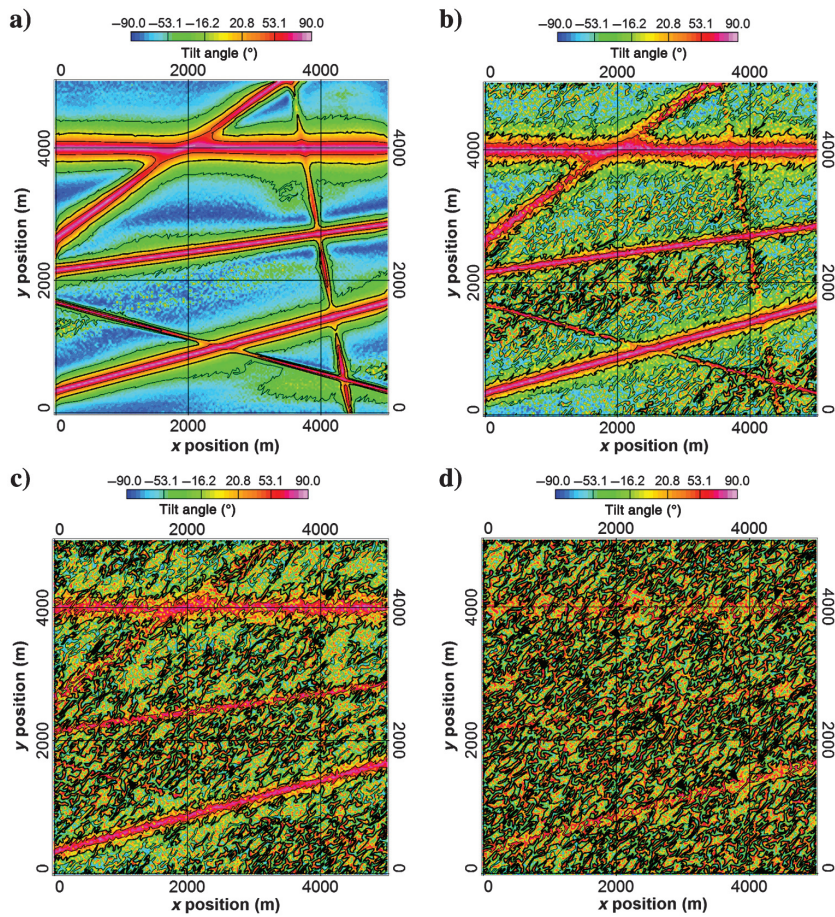


Figure 9. Contoured tilt angle results of the synthetic data sets with increasing noise levels: (a) 0.1 nT, (b) 1 nT, (c) 3 nT, and (d) 10 nT. The -45° and $+45^\circ$ contours are shown as thin black lines, whereas the 0° contours are shown as thick black lines.

the CNN approach because specific or unique anomalies may not be well-analyzed unless the training data have contained sufficiently

similar situations. As such, the established methods are still very valuable when used by experienced interpreters.

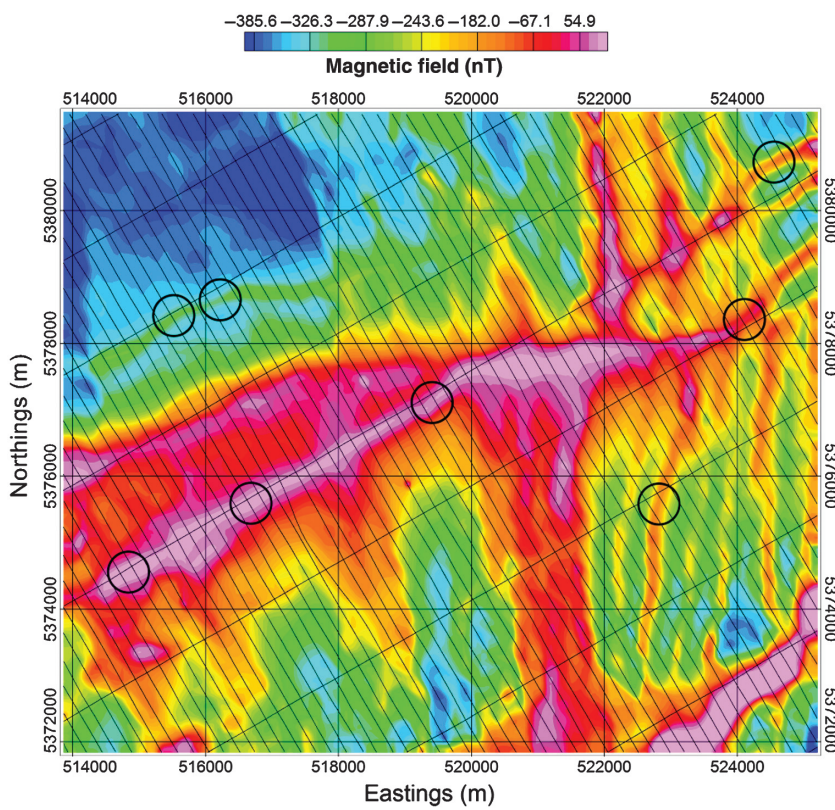


Figure 10. A subsection of the Matheson data set reduced to pole. It is centered on the dike that has been analyzed in other studies, with the eight locations of interest circled.

One of the obvious drawbacks of using a classification CNN is that continuous values cannot be predicted. This approach followed a previously successful CNN application to aeromagnetics (Nurindrawati and Sun, 2020), and it allowed for an easier training step of the process, but it results in less fidelity when analyzing data. The bins that we chose were small enough to be useful for interpretation; however, it would be understandable for the next step of this research to attempt to develop better resolution for its results, likely using a regression CNN. During this process, further experimentation of the CNN architecture may be useful, such as exploring additional activation functions, as well as new methodologies that emerge as the deep learning field continues to progress.

A primary area for future investigation is to advance this method to be able to interpret the dip of lineaments, which will likely be possible using the same general approach as for the depth. As stated previously, most dikes in Canada do not significantly deviate away from a vertical dip. However, there are still cases in which they do, and this may be an important parameter for geologic interpretation. Given enough data with varying dip angles, the CNN model may be able to predict a dike's dip to a similar accuracy as the depth can be, as shown in this paper. The primary difficulty may stem from the fact that the dip has a smaller range of realistic values as compared to the depth. The

Table 5. Comparisons between the true depths and the predicted results for the four synthetic data sets.

Anomaly	True depth	0.1 nT		1 nT		3 nT		10 nT	
		CNN method	Tilt depth	CNN method	Tilt depth	CNN method	Tilt depth	CNN method	Tilt depth
L1	100	76–100: 91% 101–125: 9%	90–110	76–100: 91% 101–125: 9%	90–100	76–100: 92% 101–125: 7% 126–150: 1%	120–125, noisy	51–75: 20% 76–100: 61% 101–125: 12%	Too noisy
L2	185	176–200: 92% 201–225: 8%	130–155	126–150: 4% 176–200: 89% 201–225: 7%	115–140	126–150: 27% 176–200: 42% 201–225: 21%	110–125, very noisy	76–100: 30% 126–150: 18% 176–200: 17%	Too noisy
L3	248	176–200: 4% 201–225: 20% 226+: 75%	215–235	176–200: 7% 201–225: 18% 226+: 74%	210–240	176–200: 12% 201–225: 15% 226+: 69%	235–245, noisy	126–150: 13% 201–225: 16% 226+: 43%	Too noisy
L4	80	25–50: 10% 51–75: 40% 76–100: 46%	50–60	51–75: 38% 76–100: 43%	50–55, very noisy	51–75: 37% 76–100: 47%	Too noisy	Too noisy	Too noisy
L5	35	26–50: 61% 51–75: 17% 76–100: 22%	30–40	26–50: 56% 51–75: 32% 76–100: 12%	35–45	101–125: 11% 101–125: 13% 76–100: 14%	26–50: 19% 51–75: 66%	Too noisy	Too noisy
L6	130	101–125: 91% 126–150: 9%	125–130	101–125: 95% 126–150: 5%	125–135	101–125: 91% 126–150: 9%	115–130	76–100: 30% 101–125: 52% 126–150: 16%	Too noisy

All lineaments contained some mix of predictions. As such, the three most common bins are shown for the CNN model depth, and a range of results is listed for the tilt depth estimates. All results are in meters.

dip of a dike will in general be no more than 30° away from vertical, except in very extreme cases. Another key area for future work is to improve the results when multiple lineaments are present because the current CNN model has difficulties when lineaments overlap. We found that the tilt depth has similar issues; however, generally for the tilt-depth method it is easiest to interpret the wider of the two

anomalies. As such, the best approach for the CNN method may be to train the model to estimate the strongest of any lineaments it detects. A possible approach to the overall improvement of this method may be to use several large synthetic data sets, similar to the synthetic model in the “Results” section, and pull subsets of data for training. This would be similar to the “patch” approach used by

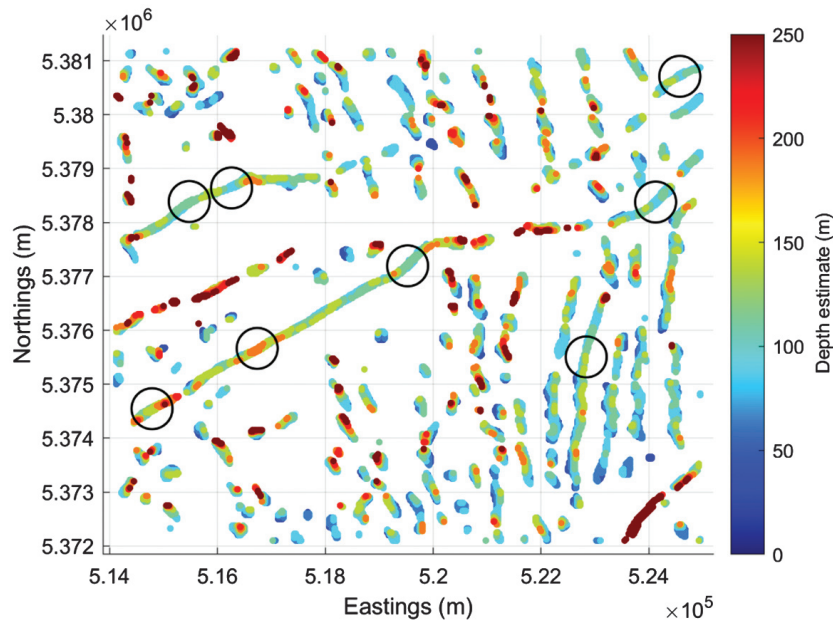


Figure 11. Predictions from the CNN model on the Matheson data set. The colorbar shows the depth estimate in steps of 25 m. The eight locations of interest are circled.

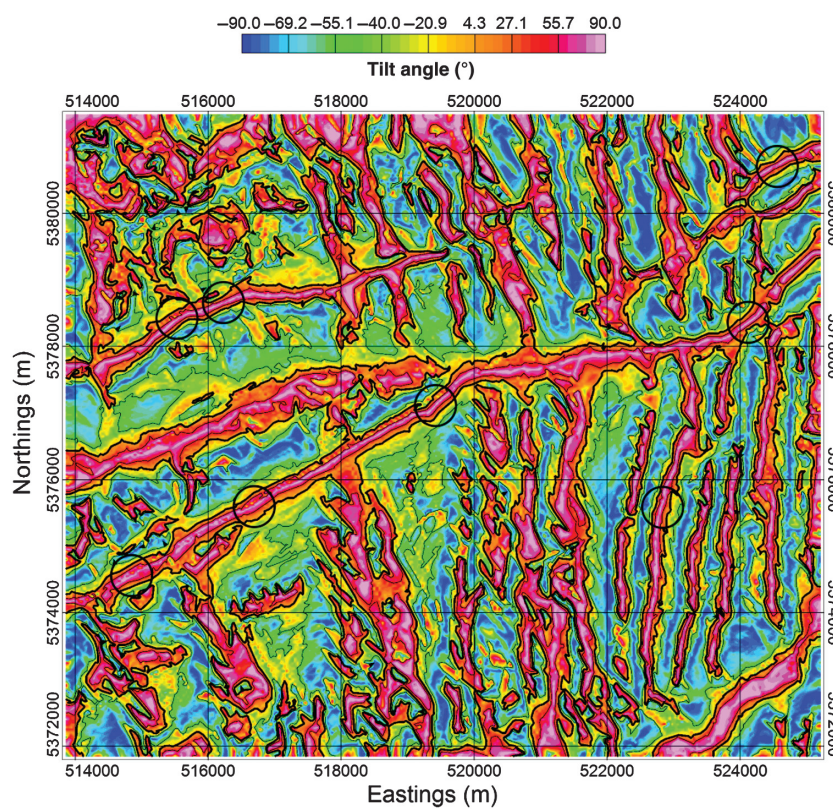


Figure 12. Contoured tilt angle results of the Matheson data set. The -45° and $+45^\circ$ contours are shown as thin black lines, whereas the 0° contours are shown as thick black lines. The eight locations of interest are circled.

Table 6. The results for both depth estimators applied to the Matheson data set at the eight locations of interest. The borehole location's true depth is given for comparison.

Anomaly	Location	CNN method	Tilt depth
Borehole (center) — 111 m	(E519470 m, N5377100 m)	100–125 m	106 m
Northwest–west location	(E515500 m, N5378400 m)	100–125 m	114 m
Northwest–east location	(E516200 m, N5378660 m)	75–100 m	88 m
Southwest–west location	(E514825 m, N5374550 m)	125–150 m	145 m
Southwest–east location	(E516700 m, N5375600 m)	175–200 m	182 m
Northeast location	(E524540 m, N5380725 m)	75–100 m	91 m
East location	(E524090 m, N5378340 m)	75–100 m	94 m
Southeast location	(E522800 m, N5375600 m)	100–125 m	115 m

Cunha et al. (2020), and it may be advantageous in generating more complex training data. Multiple window sizes could be explored, because it is possible that different window sizes may be beneficial, as well as offer user flexibility to various data sets. In addition, each data set could be generated at multiple noise levels and with various cell sizes to ensure that the CNN models are even more robust to these two effects. Using data that has not been reduced to pole could also be attempted if that is seen to be a useful configuration. Training with real data could also be accomplished; however, this process would require several highly accurate and well-defined data sets that have been analyzed by professional interpreters to ensure a sufficiently robust model.

CONCLUSION

We have presented a new approach for the automatic depth estimation of lineaments in aeromagnetic data using a CNN. Through testing on a difficult synthetic data set, this interpretation technique was shown to be accurate and more robust to noise in aeromagnetic data when compared to the tilt-depth method. Applying the CNN method to a data set from northern Ontario, Canada, a dike's location and depth were correctly estimated, as verified by previous studies and associated borehole data. Additional lineament depths were compared against tilt-depth results, further showing the accuracy of the CNN approach. In its current state, this method is likely most useful for quickly processing large or noisy data sets because after the model has been trained it requires minimal further manual input from the user, enabling large data sets to be processed easily with the additional benefit of being highly robust to noise. Once complete, the results could be used to highlight areas for further investigation with an interpreter's experience and any additional data sets. The trained CNN model can be downloaded from the author's GitHub and can be readily applied to new data sets to estimate the location and depth to the top of dike-like features in aeromagnetic maps.

ACKNOWLEDGMENTS

We would like to thank NSERC for funding the Ph.D. that this research was a part of; Natural Resources Canada for the publicly available aeromagnetic data; R. Ernst for sharing his expertise on dikes with us; and the editor, associate editor, and reviewers whose

assistance during the review process greatly improved the quality of this paper.

DATA AND MATERIALS AVAILABILITY

The data used in the case study is referenced within the paper and can be found at the website listed.

REFERENCES

- Abadi, M., A. Agarwal, P. Barham, E. Brevdo, Z. Chen, C. Citro, G. S. Corrado, A. Davis, J. Dean, M. Devin, and S. Ghemawat, 2015, TensorFlow: Large-scale machine learning on heterogeneous systems, software available from tensorflow.org, accessed 5 September 2019.
- Aghaei Rad, M. A., 2019, Machine learning of lineaments from magnetic, gravity and elevation maps: M.S. thesis, University of British Columbia.
- Bates, M. P., and H. C. Halls, 1990, Regional variation in paleomagnetic polarity of the Matachewan dyke swarm related to the Kapuskasing Structural Zone, Ontario: Canadian Journal of Earth Sciences, **27**, 200–211, doi: [10.1139/e90-020](https://doi.org/10.1139/e90-020).
- Bishop, C. M., 1995, Neural networks for pattern recognition: Oxford University Press.
- Blakely, R. J., 1996, Potential theory in gravity and magnetic applications: Cambridge University Press.
- Cascone, L., S. Campbell, C. Green, A. Salem, and D. Fairhead, 2012, ACLAS: A new automatic method of defining potential field lineaments using coherency analysis: 82nd Annual International Meeting, SEG, Expanded Abstracts, doi: [10.1190/segam2012-1254.1](https://doi.org/10.1190/segam2012-1254.1).
- Cooper, G. R. J., 2012, The semi-automatic interpretation of magnetic dyke anomalies: Computers & Geosciences, **44**, 95–99, doi: [10.1016/j.cageo.2012.02.016](https://doi.org/10.1016/j.cageo.2012.02.016).
- Cooper, G. R. J., 2014, The automatic determination of the location, depth, and dip of contacts from aeromagnetic data: Geophysics, **79**, no. 3, J35–J41, doi: [10.1190/geo2013-0181.1](https://doi.org/10.1190/geo2013-0181.1).
- Cooper, G. R. J., 2015, Using the analytic signal amplitude to determine the location and depth of thin dikes from magnetic data: Geophysics, **80**, no. 1, J1–J6, doi: [10.1190/geo2014-0061.1](https://doi.org/10.1190/geo2014-0061.1).
- Coyle, M., R. Dumont, P. Keating, F. Kiss, and W. Miles, 2014, Geological Survey of Canada aeromagnetic surveys: Design, quality assurance, and data dissemination: Geological Survey of Canada, Open File.
- Cunha, A., A. Pochet, H. Lopes, and M. Gattass, 2020, Seismic fault detection in real data using transfer learning from a convolutional neural network pre-trained with synthetic seismic data: Computers & Geosciences, **135**, 104344, doi: [10.1016/j.cageo.2019.104344](https://doi.org/10.1016/j.cageo.2019.104344).
- Curto, J. B., T. Diniz, R. M. Vidotti, R. J. Blakely, and R. A. Fuck, 2015, Optimizing depth estimates from magnetic anomalies using spatial analysis tools: Computers & Geosciences, **84**, 1–9, doi: [10.1016/j.cageo.2015.07.018](https://doi.org/10.1016/j.cageo.2015.07.018).
- de Barros, A., S. Bongiolo, J. de Souza, F. J. F. Ferreira, and L. G. de Castro, 2013, Grav mag prism: A MATLAB/octave program to generate gravity and magnetic anomalies due to rectangular prismatic bodies: Brazilian Journal of Geophysics, **31**, 347–363, doi: [10.22564/rbgt.v31i3.310](https://doi.org/10.22564/rbgt.v31i3.310).
- De Souza, J., S. P. Oliveira, and F. J. F. Ferreira, 2020, Using parity decomposition for interpreting magnetic anomalies from dikes having arbitrary dip angles, induced and remanent magnetization: Geophysics, **85**, no. 3, J51–J58, doi: [10.1190/geo2019-0225.1](https://doi.org/10.1190/geo2019-0225.1).
- Ernst, R. E., 2014, Large igneous provinces: Cambridge University Press.
- Ernst, R. E., J. W. Head, E. Parfitt, E. Grosfils, and L. Wilson, 1995, Giant radiating dyke swarms on Earth and Venus: Earth-Science Reviews, **39**, 1–58, doi: [10.1016/0012-8225\(95\)00017-5](https://doi.org/10.1016/0012-8225(95)00017-5).
- Fairhead, J. D., and S. Williams, 2006, Evaluating normalized magnetic derivatives for structural mapping: 76th Annual International Meeting, SEG, Expanded Abstracts, 845–848, doi: [10.1190/1.2370388](https://doi.org/10.1190/1.2370388).
- Ferreira, F. J. F., J. de Souza, A. B. E. S. Bongiolo, and L. G. de Castro, 2013, Enhancement of the total horizontal gradient of magnetic anomalies using the tilt angle: Geophysics, **78**, no. 3, J33–J41, doi: [10.1190/geo2011-0441.1](https://doi.org/10.1190/geo2011-0441.1).
- Foks, N. L., and Y. Li, 2016, Automatic boundary extraction from magnetic field data using triangular meshes: Geophysics, **81**, no. 3, J47–J60, doi: [10.1190/geo2015-0112.1](https://doi.org/10.1190/geo2015-0112.1).
- Geosoft Inc., 2020, Oasis Montaj, <https://www.sequent.com/products-solutions/geosoft-oasis-montaj>, accessed 18 October 2021.

- Hidalgo-Gato, M. C., and V. C. Barbosa, 2015, Edge detection of potential-field sources using scale-space monogenic signal: Fundamental principles: *Geophysics*, **80**, no. 5, J27–J36, doi: [10.1190/geo2015-0025.1](https://doi.org/10.1190/geo2015-0025.1).
- Holden, E. J., J. C. Wong, P. Kovesi, D. Wedge, M. Dentith, and L. Bagas, 2012, Identifying structural complexity in aeromagnetic data: An image analysis approach to greenfields gold exploration: *Ore Geology Reviews*, **46**, 47–59, doi: [10.1016/j.oregeorev.2011.11.002](https://doi.org/10.1016/j.oregeorev.2011.11.002).
- Hood, P., 1965, Gradient measurements in aeromagnetic surveying: *Geophysics*, **30**, 891–902, doi: [10.1190/1.1439666](https://doi.org/10.1190/1.1439666).
- TensorFlow, 2020, Keras Losses — Sparse Categorical Cross Entropy, https://www.tensorflow.org/api_docs/python/tf/keras/losses/SparseCategoricalCrossentropy, accessed 28 July 2020.
- Krizhevsky, A., I. Sutskever, and G. E. Hinton, 2012, ImageNet classification with deep convolutional neural networks: *Advances in Neural Information Processing Systems*, 1097–1105.
- Lee, M., W. Morris, J. Harris, and G. Leblanc, 2012, An automatic network-extraction algorithm applied to magnetic survey data for the identification and extraction of geologic lineaments: *The Leading Edge*, **31**, 26–31, doi: [10.1190/1.3679324](https://doi.org/10.1190/1.3679324).
- Miller, H. G., and V. Singh, 1994, Potential field tilt — A new concept for location of potential field sources: *Journal of Applied Geophysics*, **32**, 213–217, doi: [10.1016/0926-9851\(94\)90022-1](https://doi.org/10.1016/0926-9851(94)90022-1).
- Nabighian, M. N., 1972, The analytic signal of two-dimensional magnetic bodies with polygonal cross-section: Its properties and use for automated anomaly interpretation: *Geophysics*, **37**, 507–517, doi: [10.1190/1.1440276](https://doi.org/10.1190/1.1440276).
- Nair, V., and G. E. Hinton, 2010, Rectified linear units improve restricted Boltzmann machines: 27th International Conference on Machine Learning, IMLN, 807–814.
- Naprstek, T., and R. S. Smith, 2019, A new method for interpolating linear features in aeromagnetic data: *Geophysics*, **84**, no. 3, JM15–JM24, doi: [10.1190/geo2018-0156.1](https://doi.org/10.1190/geo2018-0156.1).
- Nathan, D., A. Aitken, E. J. Holden, and J. Wong, 2020, Imaging sedimentary basins from high-resolution aeromagnetics and texture analysis: *Computers & Geosciences*, **136**, 104396, doi: [10.1016/j.cageo.2019.104396](https://doi.org/10.1016/j.cageo.2019.104396).
- Nurindrawati, F. D., and J. Sun, 2020, Predicting total magnetization directions using convolutional neural networks: *Journal of Geophysical Research, Solid Earth*, **125**, e2020JB019675, doi: [10.1029/2020JB019675](https://doi.org/10.1029/2020JB019675).
- Oliveira, S. P., F. J. Ferreira, and J. de Souza, 2017, EdgeDetectPFI: An algorithm for automatic edge detection in potential field anomaly images — Application to dike-like magnetic structures: *Computers & Geosciences*, **103**, 80–91, doi: [10.1016/j.cageo.2017.02.006](https://doi.org/10.1016/j.cageo.2017.02.006).
- Ontario Geological Survey, 2003, Ontario airborne geophysical surveys, magnetic and electromagnetic data, Matheson area, Geophysical data set 1101 — Revised, <http://www.ontario.mndm.gov.on.ca/mndmfiles/pub/data/records/GDS1101.html>, accessed 24 January 2020.
- Peters, B., E. Haber, and J. Granek, 2019, Neural networks for geophysicists and their application to seismic data interpretation: *The Leading Edge*, **38**, 534–540, doi: [10.1190/tle38070534.1](https://doi.org/10.1190/tle38070534.1).
- Phillips, J. D., 2000, Locating magnetic contacts: A comparison of the horizontal gradient, analytic signal, and local wavenumber methods: 70th Annual International Meeting, SEG, Expanded Abstracts, 402–405, doi: [10.1190/1.1816078](https://doi.org/10.1190/1.1816078).
- Pilkington, M., and P. B. Keating, 2009, The utility of potential field enhancements for remote predictive mapping: *Canadian Journal of Remote Sensing*, **35**, S1–S11, doi: [10.5589/m09-021](https://doi.org/10.5589/m09-021).
- Pilkington, M., and W. R. Roest, 1998, Removing varying directional trends in aeromagnetic data: *Geophysics*, **63**, 446–453, doi: [10.1190/1.1444345](https://doi.org/10.1190/1.1444345).
- Pilkington, M., and V. Tschirhart, 2017, Practical considerations in the use of edge detectors for geologic mapping using magnetic data: *Geophysics*, **82**, no. 3, J1–J8, doi: [10.1190/geo2016-0364.1](https://doi.org/10.1190/geo2016-0364.1).
- Pochet, A., P. H. Diniz, H. Lopes, and M. Gattass, 2018, Seismic fault detection using convolutional neural networks trained on synthetic post-stacked amplitude maps: *IEEE Geoscience and Remote Sensing Letters*, **16**, 352–356, doi: [10.1109/LGRS.2018.2875836](https://doi.org/10.1109/LGRS.2018.2875836).
- Poulton, M. M., 2002, Neural networks as an intelligence amplification tool: A review of applications: *Geophysics*, **67**, 979–993, doi: [10.1190/1.1484539](https://doi.org/10.1190/1.1484539).
- Puzeyrev, V., and A. Swidinsky, 2021, Inversion of 1D frequency- and time-domain electromagnetic data with convolutional neural networks: *Computers & Geosciences*, **149**, 104681, doi: [10.1016/j.cageo.2020.104681](https://doi.org/10.1016/j.cageo.2020.104681).
- Reeves, C., 2005, Aeromagnetic surveys principles: Practice and interpretation: *GeoSoft*.
- Reid, A. B., J. M. Allsop, H. Granser, A. T. Millett, and I. W. Somerton, 1990, Magnetic interpretation in three dimensions using Euler deconvolution: *Geophysics*, **55**, 80–91, doi: [10.1190/1.1442774](https://doi.org/10.1190/1.1442774).
- Reid, A. B., and J. B. Thurston, 2014, The structural index in gravity and magnetic interpretation: Errors, uses, and abuses: *Geophysics*, **79**, no. 4, J61–J66, doi: [10.1190/geo2013-0235.1](https://doi.org/10.1190/geo2013-0235.1).
- Riesenhuber, M., and T. Poggio, 1999, Hierarchical models of object recognition in cortex: *Nature Neuroscience*, **2**, 1019–1025, doi: [10.1038/14819](https://doi.org/10.1038/14819).
- Roest, W. R., J. Verhoef, and M. Pilkington, 1992, Magnetic interpretation using the 3-D analytic signal: *Geophysics*, **57**, 116–125, doi: [10.1190/1.1443174](https://doi.org/10.1190/1.1443174).
- Ruffman, A., and J. D. Greenough, 1990, The Weekend dykes, a newly recognized mafic dyke swarm on the eastern shore of Nova Scotia, Canada: *Canadian Journal of Earth Sciences*, **27**, 644–648, doi: [10.1139/e90-061](https://doi.org/10.1139/e90-061).
- Saikia, P., R. D. Baruah, S. K. Singh, and P. K. Chaudhuri, 2020, Artificial neural networks in the domain of reservoir characterization: A review from shallow to deep models: *Computers & Geosciences*, **135**, 104357, doi: [10.1016/j.cageo.2019.104357](https://doi.org/10.1016/j.cageo.2019.104357).
- Salem, A., D. Ravat, R. Smith, and K. Ushijima, 2005, Interpretation of magnetic data using an enhanced local wavenumber (ELW) method: *Geophysics*, **70**, no. 2, L7–L12, doi: [10.1190/1.1884828](https://doi.org/10.1190/1.1884828).
- Salem, A., S. Williams, J. D. Fairhead, D. Ravat, and R. Smith, 2007, Tilt-depth method: A simple depth estimation method using first-order magnetic derivatives: *The Leading Edge*, **26**, 1502–1505, doi: [10.1190/1.2821934](https://doi.org/10.1190/1.2821934).
- Salem, A., S. Williams, D. Fairhead, R. Smith, and D. Ravat, 2008, Interpretation of magnetic data using tilt-angle derivatives: *Geophysics*, **73**, no. 1, L1–L10, doi: [10.1190/1.2799992](https://doi.org/10.1190/1.2799992).
- Scherer, D., A. Müller, and S. Behnke, 2010, Evaluation of pooling operations in convolutional architectures for object recognition: 20th International Conference on Artificial Neural Networks, ENNS, Proceedings, 92–101.
- Shi, Y., X. Wu, and S. Fomel, 2018, Automatic salt-body classification using a deep convolutional neural network: 88th Annual International Meeting, SEG, Expanded Abstracts, 1971–1975, doi: [10.1190/segam2018-2997304.1](https://doi.org/10.1190/segam2018-2997304.1).
- Simard, P. Y., D. Steinkraus, and J. C. Platt, 2003, Best practices for convolutional neural networks applied to visual document analysis: 7th International Conference on Document Analysis and Recognition, IEEE, Proceedings, 958–963.
- Smith, R. S., and A. Salem, 2005, Imaging depth, structure, and susceptibility from magnetic data: The advanced source-parameter imaging method: *Geophysics*, **70**, no. 4, L31–L38, doi: [10.1190/1.1990219](https://doi.org/10.1190/1.1990219).
- Srivastava, N., G. Hinton, A. Krizhevsky, I. Sutskever, and R. Salakhutdinov, 2014, Dropout: A simple way to prevent neural networks from overfitting: *The Journal of Machine Learning Research*, **15**, 1929–1958.
- Sun, Y., W. Yang, X. Zeng, and Z. Zhang, 2016, Edge enhancement of potential field data using spectral moments: *Geophysics*, **81**, no. 1, G1–G11, doi: [10.1190/geo2014-0430.1](https://doi.org/10.1190/geo2014-0430.1).
- The Mathworks Inc., 2020, MATLAB, <https://www.mathworks.com/products/matlab.html>, accessed 18 October 2021.
- Thompson, D. T., 1982, EULDPH: A new technique for making computer-assisted depth estimates from magnetic data: *Geophysics*, **47**, 31–37, doi: [10.1190/1.1441278](https://doi.org/10.1190/1.1441278).
- Thurston, J., and R. Smith, 2007, Source location using total-field homogeneity: Introducing the SLUTH method for depth estimation: *The Leading Edge*, **26**, 1272–1277, doi: [10.1190/1.2794385](https://doi.org/10.1190/1.2794385).
- Thurston, J. B., and R. S. Smith, 1997, Automatic conversion of magnetic data to depth, dip, and susceptibility contrast using the SPI (TM) method: *Geophysics*, **62**, 807–813, doi: [10.1190/1.1444190](https://doi.org/10.1190/1.1444190).
- Tontini, F. C., R. J. Blakely, V. Stagpoole, and H. Seebeck, 2018, Semi-automatic determination of dips and depths of geologic contacts from magnetic data with application to the Turi Fault System, Taranaki Basin, New Zealand: *Journal of Applied Geophysics*, **150**, 67–73, doi: [10.1016/j.jappgeo.2018.01.001](https://doi.org/10.1016/j.jappgeo.2018.01.001).
- Tschirhart, P., and B. Morris, 2012, Grenville age deformation of the Sudbury impact structure: Evidence from magnetic modelling of the Sudbury diabase dyke swarm: *Terra Nova*, **24**, 213–220, doi: [10.1111/j.1365-3121.2011.01056.x](https://doi.org/10.1111/j.1365-3121.2011.01056.x).
- Tschirhart, P., and B. Morris, 2015, Improved edge detection mapping through stacking and integration: A case study in the Bathurst Mining Camp: *Geophysical Prospecting*, **63**, 283–295, doi: [10.1111/1365-2478.12188](https://doi.org/10.1111/1365-2478.12188).
- Ulla, J., R. Smith, C. Samson, and M. Vallée, 2010, Automation of the SLUTH method: A novel approach to airborne magnetic data interpretation: *Near Surface Geophysics*, **8**, 519–528, doi: [10.3997/1873-0604.2010033](https://doi.org/10.3997/1873-0604.2010033).
- Vallée, M. A., P. Keating, R. S. Smith, and C. St-Hilaire, 2004, Estimating depth and model type using the continuous wavelet transform of magnetic data: *Geophysics*, **69**, 191–199, doi: [10.1190/1.1649387](https://doi.org/10.1190/1.1649387).
- Verduzco, B., J. D. Fairhead, C. M. Green, and C. MacKenzie, 2004, New insights into magnetic derivatives for structural mapping: *The Leading Edge*, **23**, 116–119, doi: [10.1190/1.1651454](https://doi.org/10.1190/1.1651454).
- Waldehand, A. U., and A. H. S. S. Solberg, 2017, Salt classification using deep learning: 79th Annual International Conference and Exhibition, EAGE, Extended Abstracts, doi: [10.3997/2214-4609.201700918](https://doi.org/10.3997/2214-4609.201700918).
- Yang, L., and S. Z. Sun, 2020, Seismic horizon tracking using a deep convolutional neural network: *Journal of Petroleum Science and Engineering*, **187**, 106709, doi: [10.1016/j.petrol.2019.106709](https://doi.org/10.1016/j.petrol.2019.106709).
- Zhang, Q., A. Yusifov, C. Joy, Y. Shi, and X. Wu, 2019, FaultNet: A deep CNN model for 3D automated fault picking: 89th Annual International Meeting, SEG, Expanded Abstracts, 2413–2417, doi: [10.1190/segam2019-3215930.1](https://doi.org/10.1190/segam2019-3215930.1).

Biographies and photographs of the authors are not available.